**International Invention of Scientific Journal**
Online ISSN: 2457-0958
Available Online at https://iisj.in **Volume 8, Issue 03 (July-August-September)|2024**|Page: 390-401
Original Research Paper-Engineering

# Designing and Simulating a ±16g Micromachined Accelerometer with Enhanced Parameters for Automotive Navigation

**Authors:**
**Masoud Akbarzadeh Asl[1]*, Saeed Afarang[2]**
[1]*M.Sc., Department of Electrical Engineering, Urmia University, Urmia, Iran*
[2]*Faculty Member, Department of Electrical Engineering, Urmia University, Urmia, Iran*
**Corresponding Author**:
Masoud Akbarzadeh Asl
M.Sc., Department of Electrical Engineering, Urmia University, Urmia, Iran

Article Received: 26-May-2024 Revised: 16-June-2024 Accepted: 06-July-2024

**ABSTRACT**:
This research aims to design and simulate a single-axis capacitive accelerometer using surface micromachining technology for detecting accelerations in the range of ±16g, with applications in automotive navigation systems. The overall dimensions of the accelerometer are $1mm^2$, , its initial capacitance is $1836fF$, its capacitance sensitivity is $544fF/g$, and its resolution is $3.8628\,\mu g/\sqrt{Hz}$. To reduce the effects of residual stress, a fully symmetric structure is employed. Considering the pull-in phenomenon and innovative spring design, the maximum displacement of the moving mass is utilized to enhance the capacitance, ensuring that the system operates within the linear range. The proposed structure's advantages include the use of a differential structure to eliminate environmental noise and linearize the output. Due to the single-axis nature of the accelerometer, appropriate spring design prevents axis interference during acceleration measurement. The implementation of surface micromachining technology enables the simultaneous fabrication of the accelerometer and its processing circuit on a single die. This approach reduces manufacturing costs while improving sensor accuracy and sensitivity. The design and simulation of the proposed accelerometer were carried out using COMSOL Multiphysics 5.6 and MATLAB software.

***Keywords: Capacitive accelerometer, surface micromachining, COMSOL software, MATLAB software***

## INTRODUCTION:

Accelerometers are among the first and most widely used MEMS structures, and extensive research has been conducted on them over the past few decades, leading to the design and fabrication of various types. Therefore, the focus of all researchers in recent years has been solely on optimizing this component. Optimization includes increasing sensitivity, reducing size, reducing manufacturing costs, and increasing resistance to noise and shock (thermal, mechanical, electrical, etc.).

Not only capacitive accelerometers but also all MEMS structures that utilize the capacitive detection and excitation mechanism are limited in their stable operating region by the Pull-in phenomenon. Tuning and sensitivity enhancement methods in capacitive MEMS structures include methods that prevent or delay the occurrence of the Pull-in phenomenon. One of these methods, which has attracted the attention of many researchers and has been the subject of extensive studies in recent years, is the use of a closed-loop control system [1].

Studies conducted in the field of closed-loop control on common MEMS capacitive structures such as micromirrors (Chen, Pallapa et al. 2013), gyroscopes (Xin and Fei 2015), resonators (Sarraf, Sharma et al. 2012), capacitive ultrasonic transducers (Qin, Sun et al. 2017), variable capacitors (Mobki, Sabegh et al. 2020), and accelerometers (Fathalilou, Soltani et al. 2020, Guo, Ma et al. 2020, Goswami, Kalra et al. 2021) are focused on how to extend the range of motion of the movable electrode beyond the Pull-in instability region. However, the nonlinear behavior of the system in changes in movable electrode displacement or capacitance with respect to applied bias voltage in the region beyond Pull-in instability has not been eliminated.

The common design for excitation mode in a resonator includes a closed-loop controller that adaptively tracks the resonator's natural mechanical frequency, which can be implemented using, for example, a phase-locked loop (PLL) or a bandpass sigma-delta circuit. Raman et al. (Raman, Cretu et al. 2009) in 2009 used a sigma-delta closed-loop controller for digital control of a MEMS gyroscope. Lu in 2004 (Lu and Fedder 2004) presented a time-varying linear gain controller to control the position of a MEMS structure consisting of two parallel plates. Zhu in 2006 (Zhu, Lévine et al. 2006) proposed a Lyapunov-based nonlinear control method that allows the range of motion of the movable

electrode to be extended to 90% of the initial air gap without overshoot [3].

One of the closed-loop control methods is the sliding mode strategy. This method has been used in many control systems, and its advantage is effective control of uncertainties and external disturbances. Sarraf et al. (2012) proposed a bandpass sliding mode controller for a MEMS resonator that can track possible changes in the resonator's natural frequency caused by external factors such as humidity, temperature, pressure, acceleration, noise, and so on. Compared to phase-locked loop controllers, it has better performance and uses a simpler circuit. Qin et al. (2017) proposed a sliding mode controller to optimize the behavior of a capacitive ultrasonic transducer, which provides the ability for fast response, elimination of overshoots, and extension of the movable electrode's range of motion to 90% of the air gap. Mobki et al. (2020) applied the sliding mode controller to stabilize a MEMS variable capacitor. In this study, the proposed control method was used to optimize the performance of a micromachined variable capacitor with two parallel plates (one movable and one fixed), so that the maximum capacitance and tunability of the structure were increased by stabilizing the movable electrode against the fixed electrode.

Since MEMS capacitive structures operate in both mechanical and electrical energy domains, there are two ways to extend their stable operating range. As discussed in the previous paragraphs, a closed-loop control system is a method used to extend the stable operating range of the structure in the electrical domain. This method has good performance, high accuracy, and very good sensitivity, but the main problem with using a closed-loop control method is the difficulty of implementation. It is also very expensive and requires a complex circuit. Therefore, researchers are looking for another method to control the Pull-in phenomenon without the help of a circuit and a closed-loop control system, which is control in the mechanical energy domain. In this way, this capability is inherently embedded in the structure during the manufacturing process through appropriate design, so that optimization can be achieved to increase sensitivity and reduce the effect of the Pull-in phenomenon. Mechanical control methods include the use of nonlinear springs (Nguyen, Halvorsen et al. 2010, Ghasemi, Afrang et al. 2020, Guo, Ma et al. 2020) and the two-mass model (Sotoudeh 2018, Fathalilou, Soltani et al. 2020).

Inertial navigation systems (INS) are among the most critical components for determining the position, velocity, and attitude of moving vehicles. Traditional navigation accelerometers include bulky electromagnetic accelerometers and quartz vibration accelerometers. While electromagnetic accelerometers offer high performance, they are expensive and fragile. On the other hand, quartz vibration sensors have a wide dynamic range but suffer from high cost and instability after shocks in high-shock and high-vibration environments. Microelectromechanical systems (MEMS) fabrication technology presents an excellent potential for enhancing performance in the field of navigation. This study focuses on the design and simulation of a MEMS accelerometer for improved performance parameters targeting inertial navigation applications. The primary objectives are to reduce cost, size, and power consumption compared to traditional accelerometers using MEMS technology, while the main goal is to enhance the accelerometer's performance parameters.

## Proposed Structure:

Accelerometer design typically involves two main stages: analytical design and simulation. The analytical design stage, also known as the theoretical design stage, utilizes the mathematical equations governing the structure. MATLAB software is employed for optimization during this phase. The simulation stage is conducted using finite element analysis in COMSOL Multiphysics software. In the analytical design stage, the dynamic measurement range of acceleration and the required accuracy are first determined and targeted based on the accelerometer's application. The appropriate fabrication technology and materials are then selected accordingly, followed by structural design. The structural design is further divided into three main components of the accelerometer: the moving mass, springs, and electrodes. Since the accelerometer designed in this study is intended for automotive and autonomous navigation systems [1], the measurable acceleration range of the proposed structure is within ±16 g with a bandwidth exceeding 300 Hz and an accuracy within 0.1 mg (Zwahlen, Nguyen et al., 2010). The structural materials must possess high mechanical strength. Based on the conducted studies, suitable materials include single-crystal silicon, polysilicon, aluminum, gold, and nickel. The accelerometer in this research is single-axis and designed for the range of ±16 g for application in automotive auto-routing systems. A capacitive detection mechanism with a differential air-gap variable comb capacitor structure is employed in the design. The schematic of the differential accelerometer structure is shown in Figure 1. The overall 3D view of the designed accelerometer is also presented in Figure 2.

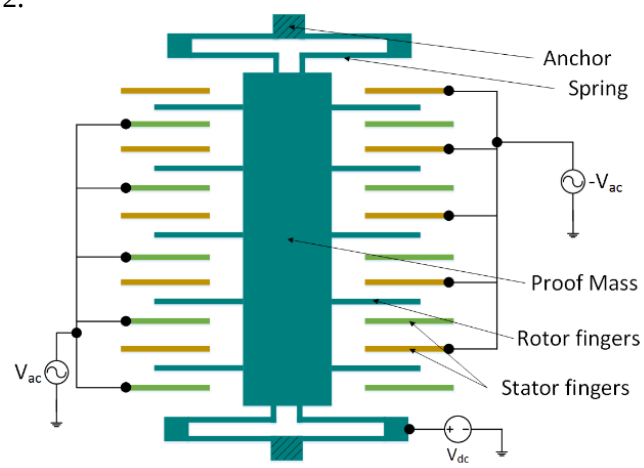

Figure 1. Schematic of differential capacitive accelerometer with shoulder capacitor

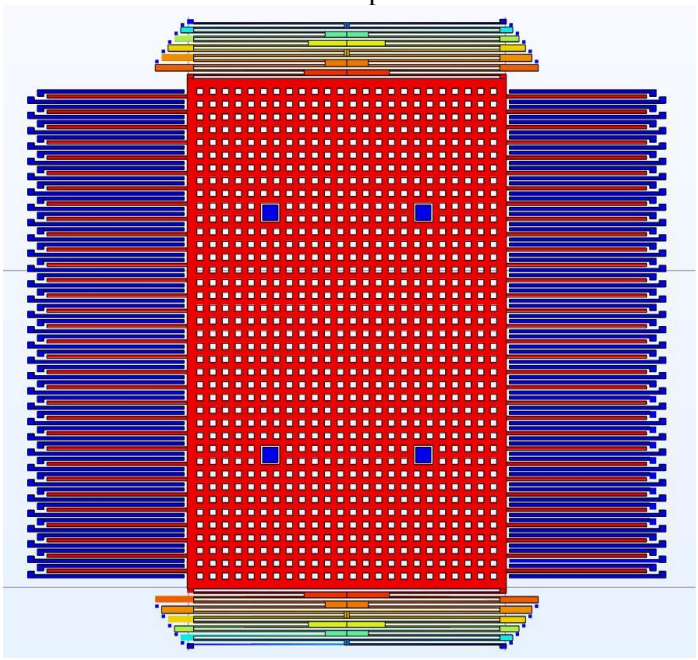

Figure 2. An overview of the accelerometer designed in this research

The accelerometer structure design process consists of three main parts: moving mass design, electrode design, and spring design. To optimize the accelerometer structure compared to similar research, the goal is to keep the overall structure dimensions within $1mm^2$.

Following the initial design, it was determined that the spring constant obtained in proportion to the assumed moving mass was not sufficient for spring design. In other words, the small effective mass resulted in a small spring constant, and consequently, the spring dimensions became so small that the system would be susceptible to unwanted accelerations. Therefore, during the optimization process, using MATLAB software and creating a competition between the dimensions of the moving mass, spring constant, and number of electrodes, the final characteristics of the moving mass were obtained as shown in Table 1. The difference between the effective mass obtained from the theoretical method and COMSOL software is due to the negligence of the spring mass, which is added to the total moving mass.

Table 1. Dimensions and Specifications of the Moving Mass

| Parameter | Symbol | Value |
|---|---|---|
| Width of the proof mass | $W_m$ | $500\mu m$ |
| Length of the proof mass | $L_m$ | $800\mu m$ |
| Device thickness | $t$ | $10\mu m$ |
| Size of the etch holes | | $10\mu m \times 10\mu m$ |
| Gap between holes | | $10\mu m$ |
| Analytical calculation of effective mass | $M_{eff}$ | $34.212\mu g$ |
| COMSOL calculation of effective mass | $M_{eff}$ | $36.873\mu g$ |

The electrodes are located inside the moving mass. If designed as a cantilever, with the electrodes placed on both sides of the moving mass, the number of electrodes doubles compared to the previous case, resulting in a doubling of the initial and differential capacitance. The length of the fixed electrodes is considered to be $220\mu m$ after optimization.

The dimensions and specifications of the electrodes are shown in Table 2. This table also includes the initial capacitance calculated theoretically (using the aforementioned equations) compared to the capacitance calculated using the finite element method. The small difference between these values indicates the high accuracy of the theoretical calculations and the optimized design.

Table 2. Dimensions and Specifications of the Electrodes

| Parameter | Symbol | Value |
|---|---|---|
| Width of the movable electrode (rotor) | $W_r$ | $5\mu m$ |
| Length of the movable electrode (rotor) | $L_r$ | $220\mu m$ |
| Device thickness | $t$ | $10\mu m$ |
| Width of the fixed electrode (stator) | $W_s$ | $5\mu m$ |
| Length of the fixed electrode (stator)-upside | $L_{su}$ | $230\mu m$ |
| Length of the fixed electrode (stator)-downside | $L_{sd}$ | $245\mu m$ |
| Initial gap between electrodes | $g_0$ | $3\mu m$ |
| Total number of sensing fingers | $N$ | 64 |
| Analytical calculation of initial capacitance | $C_0$ | $1823fF$ |
| COMSOL calculation of initial capacitance | $C_0$ | $1836fF$ |

The spring design plays a crucial and sensitive role in the accelerometer under study. The innovative spring design, explained in detail in this section, contributes to optimal accelerometer performance, enhancing efficiency and sensitivity without requiring additional control circuitry or complex mechanical structures. In contrast to intricate designs presented in other researchers' studies, this study employs a conventional capacitive accelerometer structure to simplify implementation. Linear springs are used in the spring section, enabling the design approach to be readily extended to other capacitive-mechanism structures.

Due to the use of linear springs, the structure's mechanical behavior can be modeled using the lumped-mass model, as represented by equation (1). Considering the Pull-in phenomenon, the maximum displacement of the moving mass to achieve linear capacitance changes is limited to $\frac{1}{3}$ of the air gap considered in the electrode design. This limitation arises from the decreasing spring stiffness with increasing displacement of the moving mass. The rewritten form of equation (1) is given as follows:

$$M_{eff}\ddot{y} + B\dot{y} + K_m y = F_a + F_e \quad (1)$$

In this equation, $y$ represents the displacement of the moving mass along the horizontal axis, $M_{eff}$ is the effective mass of the moving part, $B$ is the damping

coefficient of the system, $K_m$ is the mechanical stiffness coefficient of the system, $F_e$ is the equivalent force corresponding to the acceleration applied to the structure, and $F_a$ is the force resulting from the electrical potential difference between the electrodes. The equation can be rewritten as follows:

$$F_a = M_{eff} * acceleration * g_{const} \quad (2)$$

where $g_{const}$ represents the acceleration due to gravity, which is approximately $9.8\, m.s^{-2}$.The force resulting from the electrical potential difference between the electrodes can be derived based on the energy stored in the capacitor between the electrodes.

$$E_e = \frac{1}{2}C_1V^2 + \frac{1}{2}C_2V^2 = \varepsilon_0 NL_r tV^2\left(\frac{1}{g_0 - y} + \frac{1}{g_0 + y}\right) = \frac{\varepsilon_0 NL_r tV^2 g_0}{g_0^2 - y^2} \quad (3)$$

$$F_e = \frac{\partial E}{\partial y} = 2\varepsilon_0 NL_r tV^2 g_0 \frac{y}{(g_0^2 - y^2)^2} \quad (4)$$

According to equation (4), the electrical field force exhibits an inverse fourth-power relationship with the change in distance between the capacitor plates. In other words, when acceleration is applied and the moving mass displaces, assuming the potential difference between the electrodes remains constant, the electrical field force increases. This increase in force continues until the sum of the acceleration and electrical field forces equals the opposing force due to the system's stiffness coefficient.

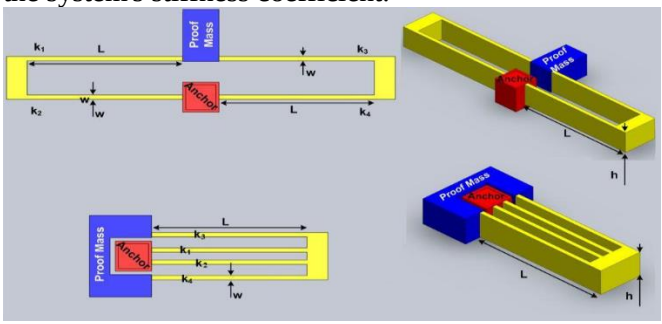

Figure 3. Folded-beam spring structure

The stiffness coefficient of one unit of folded-beam spring (Figure 3) is calculated according to the following equation.

$$K_{equal} = (k_1 series\ to\ k_2)||(k_3 series\ to\ k_4) = \left(\frac{k_1k_2}{k_1 + k_2}\right) + \left(\frac{k_3k_4}{k_3 + k_4}\right) \quad (5)$$

If the microbeams or cantilevers forming the Folded-beam spring have identical dimensions, the stiffness coefficients of all beams will be equal. Consequently, according to equation (5), the equivalent stiffness is equal to the stiffness of a single beam. As illustrated in Figure 3, the maximum displacement in this structure can be calculated based on the number of Folded-beam spring units (n) employed.

$$y_{max} = \left(1 - \left(\frac{2}{3}\right)^n\right) g_0 \quad (6)$$

Thus, the amount of tuning expected from the design based on the displacement of the moving mass will be equal to:

$$\%tuning\ ratio = \frac{y_{max}}{g_0} * 100 \quad (7)$$

Table (3) shows the dimensions and specifications of the springs used in the studied accelerometer structure after optimization by MATLAB software.

| Parameter | Length | Width | Stiffness |
|---|---|---|---|
| $K_1$ | $236\mu m$ | $2\mu m$ | $2.6658N.m^{-1}$ |
| $K_2$ | $206\mu m$ | $2\mu m$ | $4.0083N.m^{-1}$ |
| $K_3$ | $180\mu m$ | $2\mu m$ | $6.0082N.m^{-1}$ |
| $K_4$ | $236\mu m$ | $3\mu m$ | $8.9971N.m^{-1}$ |
| $K_5$ | $206\mu m$ | $3\mu m$ | $13.5281N.m^{-1}$ |
| $K_6$ | $173\mu m$ | $2\mu m$ | $6.7675N.m^{-1}$ |

**Results**

**1. Accelerometer Performance in the Main Axis Direction**

After designing and setting appropriate boundary conditions in COMSOL software, we first investigated the accelerometer's performance in the main axis direction without considering the stoppers. The goal was to compare the results with those obtained from theoretical analysis and validate the design process. Since the design utilizes six sets of springs, the accelerometer's performance is evaluated for an acceleration equal to one-sixth of the total intended acceleration range.

As shown in the figures, the displacement of the moving mass for an acceleration of 2.66g in the main axis direction was first calculated using Solid Mechanics physics. Initially, an acceleration of 2.66g was applied to the structure consisting of six sets of springs in series (K1 to K6). According to the results, the total displacement of the moving mass is $1.07\mu m$, which is very close to the theoretical calculations.

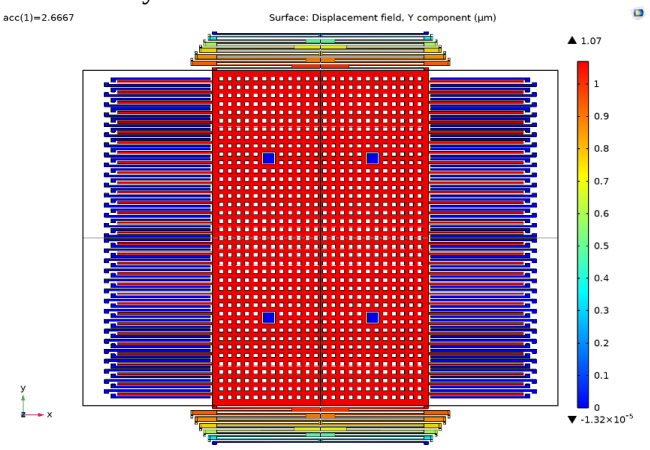

Figure 4. Displacement per acceleration of 2.66g and springs K1 to K6

Figure 5 presents a simulation similar to the previous case, but with an acceleration of 2.66g. In this scenario, spring $K_1$ is removed by fixing its end boundary, resulting in a total stiffness of the system for springs $K_2$ to $K_6$. As shown in the figure, the areas with zero displacement are indicated in dark blue, and spring $K_1$ is also represented in this color. Under these conditions, the displacement of the moving mass is $0.7\mu m$.

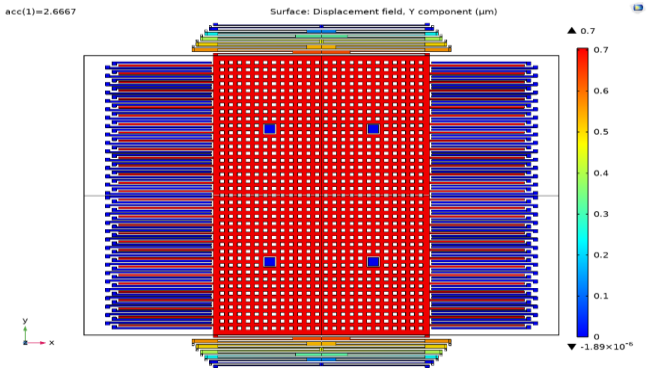


Figure 5. Displacement per acceleration of 2.66g and springs $K_2$ to $K_6$

Figures 6 to 9 illustrate the displacement of the moving mass for a constant acceleration of 2.66g. In each figure, a spring is sequentially removed ($K_2$ to $K_5$), effectively removing the stiffness contribution of that spring from the total system stiffness. As a result, the overall stiffness increases. Consistent with the results, the displacement of the moving mass decreases with each increasing overall stiffness. The close agreement between the results obtained from COMSOL finite element analysis and the theoretical calculations validates the design process and the analytical methods employed. The minimal discrepancies between the corresponding results in each stage further support the accuracy of the design and analysis approach.

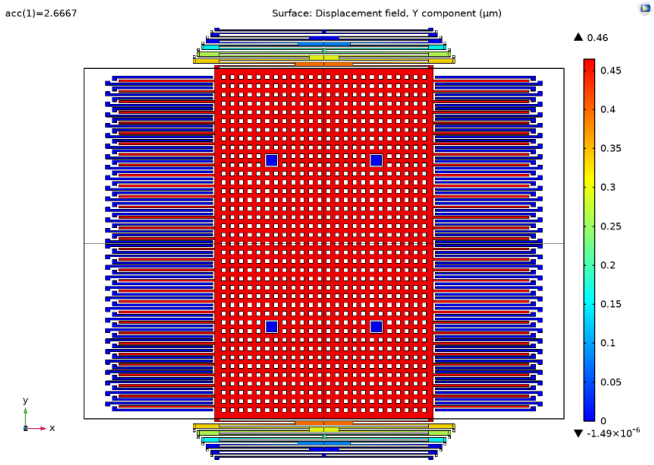


Figure 6. Displacement per acceleration of 2.66g and springs $K_3$ to $K_6$

.

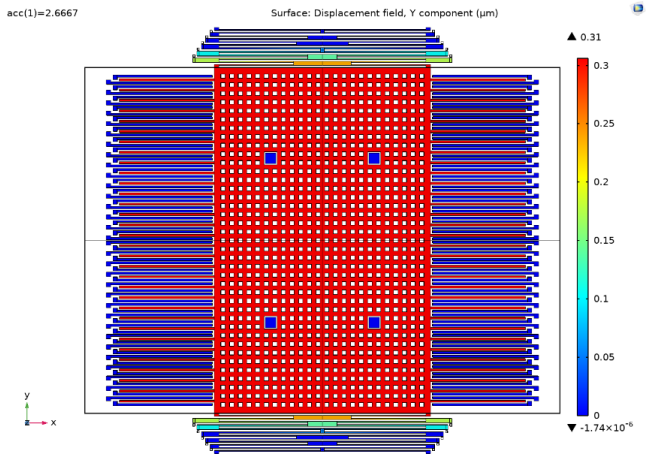


Figure 7. Displacement per acceleration of 2.66g and springs $K_4$ to $K_6$

.

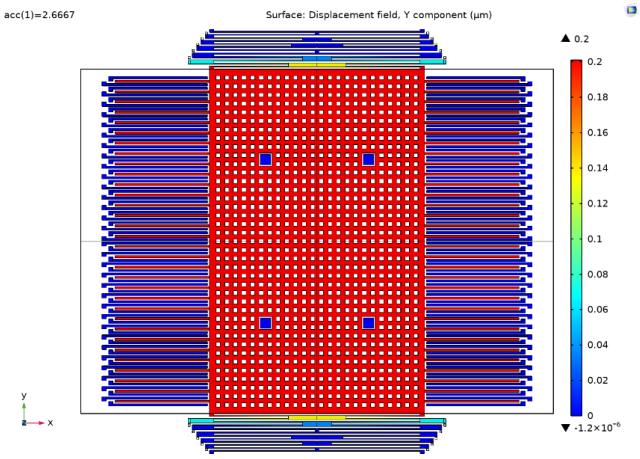


Figure 8. Displacement per acceleration of 2.66g and springs $K_5$ to $K_6$

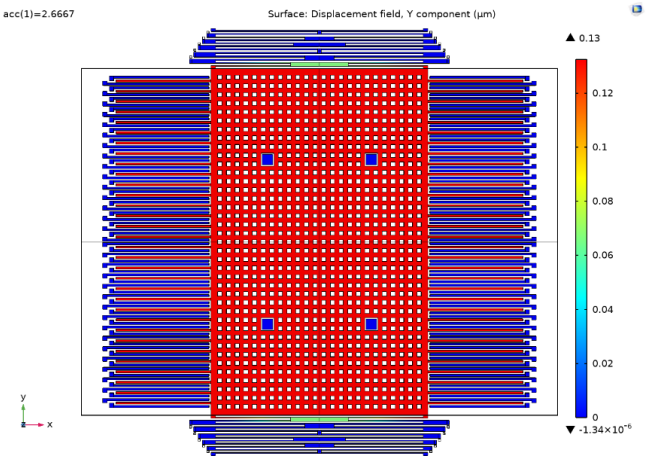


Figure 9. Displacement per acceleration of 2.66g and spring $K_6$

Up to this point, the displacement of the moving mass has been investigated for an applied acceleration of 2.66g and varying stiffness coefficients. However, the accelerometer structure under study is designed for an acceleration range of 0g to 10g, and its performance needs to be evaluated over this full range. Since the moving mass has an initial displacement due to the previous analysis and spring removal, the analytical method must account for this initial displacement. To eliminate the effect of each spring, a component called a "stopper" is incorporated into the design. A stopper is a rigid piece made from the structural body or substrate that is deposited during the fabrication process at the desired location. This piece is attached to the substrate and prevents the suspended mass from moving further upon impact. Due to the complexity of the mathematical equations governing the behavior of the suspended mass upon impact with the stopper, the performance of the proposed accelerometer structure upon impact with the designed stoppers is analyzed solely using finite element analysis. The behavior of the stoppers can be implemented in the COMSOL simulation environment using a tool called "contact pair."

The results indicate that the displacement of the moving mass varies with the displacement of each spring. These variations can be observed using the color markers placed alongside each figure. The placement of the stoppers should ensure that the moving mass stops at the predetermined displacement for each stage, preventing further displacement of the corresponding spring. The stoppers are positioned at the ends of the springs. A crucial aspect of employing the contact pair tool is the proper meshing of the structure within the contact boundaries. In other words, the meshing of the structure should be refined in the areas where the contact pair is applied to prevent analysis errors.

Since the analysis of a capacitive accelerometer involves both mechanical and electrostatic behavior, the electrostatic physics is added to the simulation environment in addition to the solid mechanics physics. Consequently, the software performs calculations simultaneously in three domains: electric field, displacement field, and contact force. This complexity necessitates advanced hardware capabilities for the analysis. One advantage of the proposed structure is its symmetry, which allows the use of the symmetric feature in the finite element environment to reduce computational load. Therefore, only one-quarter of the accelerometer structure, designed symmetrically about the x and y axes, is analyzed to simulate the overall system behavior. The results can then be extended to the entire structure.

Figure 10 illustrates the displacement of the accelerometer as the applied acceleration increases until it reaches the first stopper, which is attached to spring $K_1$, at an acceleration of 2.7g (or one-sixth of the full-scale acceleration of 16g). The resulting displacement, as shown in the figure, is $1.08\mu m$, which is very close to the previous results. According to the calculations, the structure reaches the first stopper position at an acceleration of 2.66g. However, at an acceleration of 2.7g, the contact surfaces of the stopper fully overlap, preventing further movement of the corresponding spring. Therefore, Figure 10 is shown for an acceleration of 2.7g. Figure 11 shows a zoomed-in view of the springs, clearly illustrating the complete contact of the first spring's support with the stopper. Figure 12 displays the stress distribution on the springs in the first phase of the structure's operation. As indicated in the figure, the highest stress occurs at the support of the first spring, with a value of $6MPa$, which is a negligible fraction of the yield strength of the nickel structural layer.

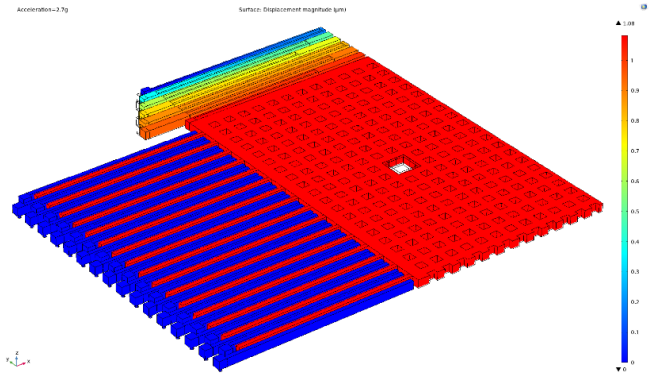

Figure 10. Displacement per acceleration of 2.7g and hitting the first stopper

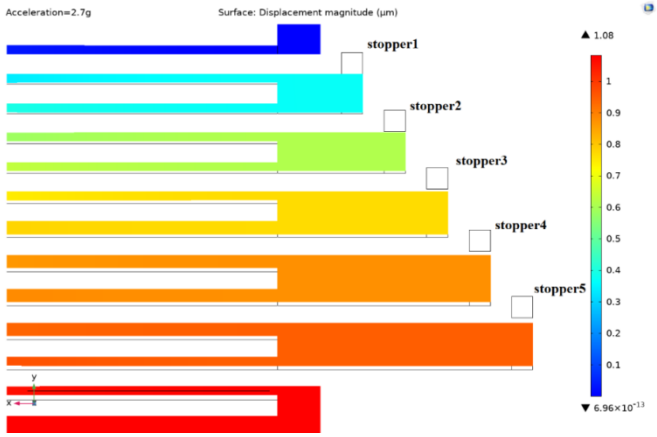


Figure 11. The support position of the springs in contact with the first stopper

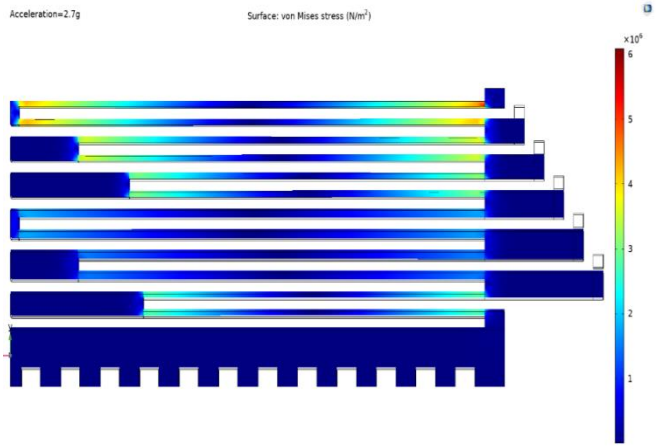


Figure 12. Stress distribution on springs at 2.7g acceleration

In the second stage, with the acceleration increasing to 5.3g along the main axis of the accelerometer, the total displacement of the moving mass is calculated to be $1.78\mu m$ (Figure 13). This value is slightly different from the $1.66\mu m$ expected from the theoretical design. This discrepancy arises from the electric field force generated between the electrodes.

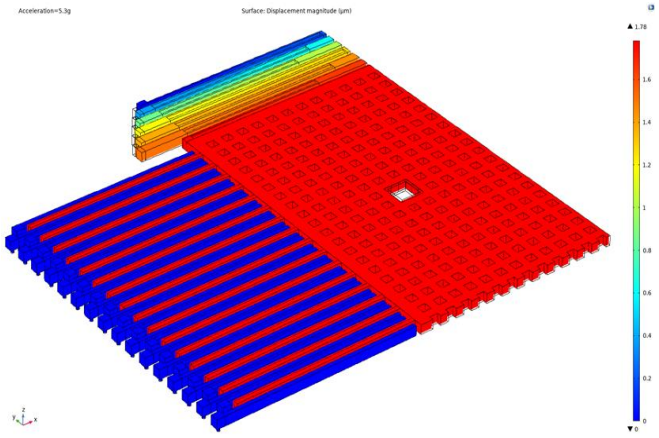

Figure 13. Displacement per acceleration of 5.3g and collision with the second stopper

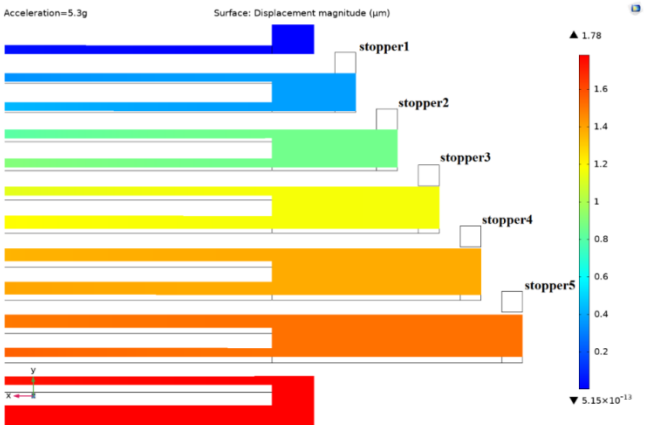


Figure 14. The support position of the springs in contact with the second stopper

As can be seen from the color-coded display in Figure (14), the displacement of the first spring after impact with the stopper remains the same as in the previous stage (no increase in displacement). The impact of the second spring with the stopper is also visible. These figures confirm the correct operation of the designed contact pair and stoppers. Figure (15) also shows an increase in stress in the springs compared to the previous stage. As can be seen in the figure, at this stage the maximum stress occurs at the connection point of the $K_2$ spring beams to the support, and the first spring does not experience an increase in stress due to the impact with the stopper and the stoppage of its movement.

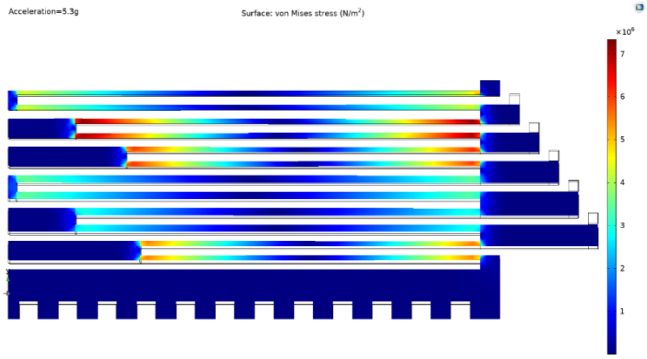


Figure 15. Stress distribution on springs at 5.3g acceleration

Since the explanations of the results in each stage are similar, the results of stages 3 to 6 were grouped for better comparison. Thus, the displacement of the movable mass assembly, electrodes, and springs was examined at accelerations of 7.94g, 10.63g, 13.35g, and 16g in the symmetric case. Since the movable mass has a rigid body mode, the displacement is the same at all points, which can be observed in all figures, where all points of the movable mass are shown in the same color. The movable electrodes are also shown in the same color due to their uniform movement with the movable mass. It should be noted that the stiffness of the electrodes, with the help of their appropriate design, resists the force caused by the electric field and prevents them from bending. Therefore, the movement of the capacitor plates is uniform along the entire length of the electrode, and there will be no error due to the bending of the electrodes in the output of the accelerometer. The results showed that the displacement of each spring is stopped after impact with the corresponding stopper, and in the next stage the equivalent stiffness of the system increases, and the displacement of the movable mass decreases for the same acceleration changes. Thus, the principle of displacement by one-third of the remaining air gap is implemented in each stage.

Figure (16) shows the displacement curve of the movable mass and the spring supports for accelerations from zero to +16g. Since the structure is designed symmetrically, the performance of the accelerometer will be the same for negative accelerations as well. Therefore, in order to reduce the computational volume and simulation time, the analysis of negative accelerations has been neglected. As can be seen in the figure, the displacement of the support of each spring is stopped after reaching the corresponding stopper, which has increased the total displacement of the accelerometer compared to conventional methods. The maximum displacement of the movable mass at 16g acceleration is equal to $2.85\mu m$.

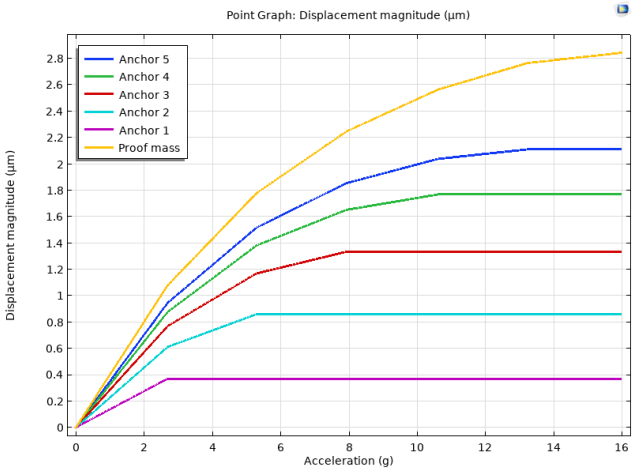


Figure 16. Moving mass displacement curve and spring support for zero to +16g acceleration

Another parameter that was investigated in the context of contacts is the force applied to the contact surfaces. Figure (17) shows the maximum pressure applied to the contact surfaces in pascals. As can be seen, after impact with the first stopper, the contact force to prevent the movement of the first spring increases

sharply until impact with the second stopper occurs. Due to the increased contact surface area caused by the second stopper and the strengthening of the retaining elements, the slope of the graph decreases and the force applied to the contact surface decreases despite the increase in acceleration. This trend is observed further in the collision with other stoppers. The reason for the sudden increase in the slope of the graph in the collision with the third stopper is due to a calculation error due to the inadequacy of the acceleration increment steps in the simulation process, which could not be increased due to hardware limitations. However, despite this calculation error and by observing other calculation results, including displacements that are in accordance with the mathematical logic governing the problem and theoretical calculations, this error can be ignored. Finally, the maximum force applied to the contacts at 16g acceleration is calculated to be 240kPa.

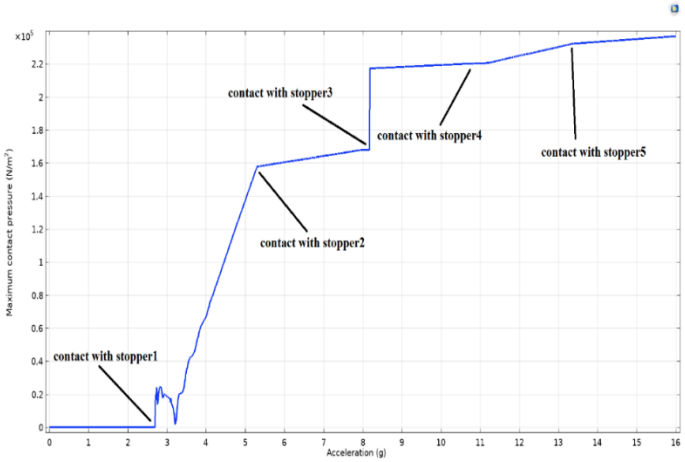


Figure 17. Contact force changes with acceleration

The changes in capacitance between the movable electrode and the fixed electrodes on both sides of the movable electrode, called Cup and Cdown, are shown in the graph in Figure (18). According to the results of finite element simulation, the initial capacitance of the proposed structure is calculated to be 1836fF. As the acceleration in the positive direction of the main axis (+y) increases, the distance between the movable electrode and the upper fixed electrode decreases, and the capacitance of Cup increases. Conversely, as the distance between the movable electrode and the lower fixed electrode increases, the capacitance of Cdown decreases. The nonlinear relationship between capacitance and distance between the plates can be clearly seen in this figure. Due to the symmetry of the accelerometer structure, the changes in capacitance for accelerations in the negative direction of the main axis (-y) are the same as the changes in the positive direction. Due to the increase in computational volume and simulation time, their calculation using the finite element method has been neglected. However, the values for negative accelerations have been added to the graph using MATLAB software and are shown with a dashed line.

The graph in Figure (19) shows the changes in differential capacitance at the output of the designed sensor for operation in the acceleration range of ±16g.

As can be seen, the nonlinear effects of air gap changes, despite the use of the maximum air gap between the electrodes to create capacitance changes, are reduced at the output using the differential mode. According to the graph, the capacitive sensitivity of the accelerometer presented in this study is calculated to be $C_s = 544fF/g$ (Equation 8).

$$C_s = \frac{\Delta C}{\Delta g} = \frac{8706fF}{16g} \cong 544fF/g \qquad (8)$$

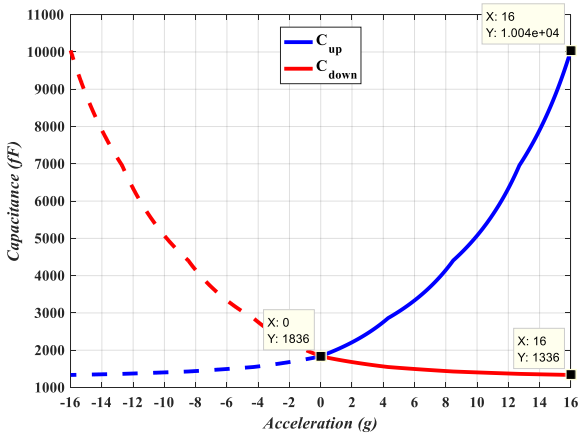


Figure 18. Capacitance changes per ±16g acceleration

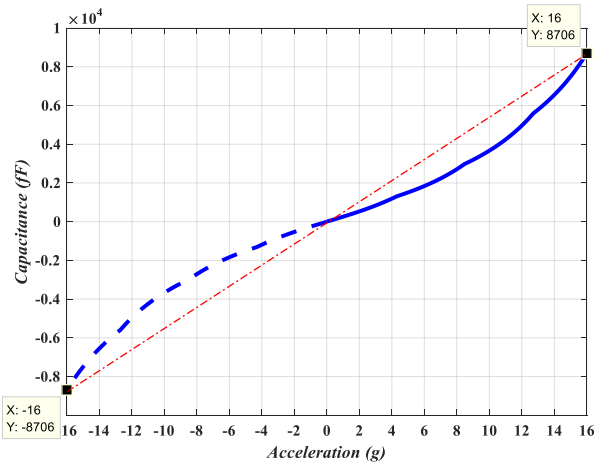


Figure 19. Differential capacitor

## Cross-Axis Sensitivity:

One of the key factors in evaluating the proper operation of an accelerometer is the impact of accelerations perpendicular to the main measurement axis on the accelerometer's behavior and output. This is known as cross-axis sensitivity. In this section, the results of finite element simulations of the accelerometer for accelerations along the x and z axes are examined.

## Horizontal Acceleration (x-axis):

In the first stage, an acceleration of 16g was applied to the accelerometer along the horizontal x-axis, which is perpendicular to the main axis. The results are as follows:

As can be seen in Figure (20), the accelerometer structure is displaced due to the applied acceleration along the x-axis. However, due to the appropriate design of the springs and the folded-beam spring structure, the stiffness in the x-direction is high and prevents excessive displacement of the structure in this

axis. Thus, the maximum displacement of the movable mass for the maximum acceleration in the accelerometer's operating range (±16g) is a small value of $0.21\mu m$. This figure also shows the bending and twisting of the springs.

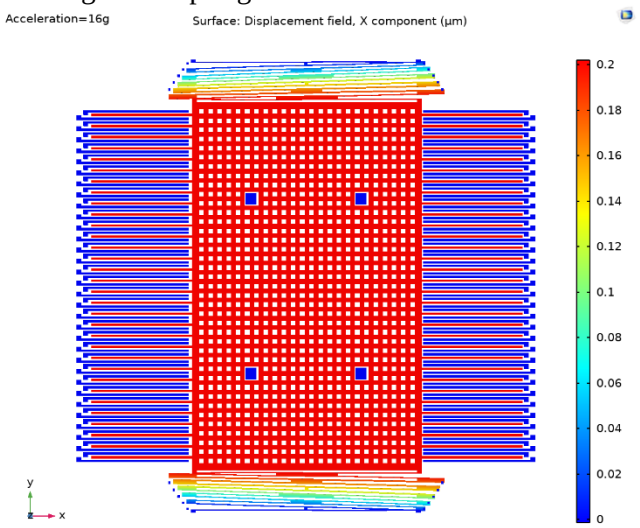


Figure 20. Displacement of moving mass per acceleration of 16g in x direction

The stiffness of the springs in the z-direction is directly proportional to the thickness of the structural layer. Therefore, the thickness of $10\mu m$ of the structural layer provides a suitable stiffness for the springs in the direction perpendicular to the substrate, which prevents excessive displacement due to unwanted accelerations in this axis. As can be seen in Figure (21), the proposed structure is displaced by $1.21\mu m$ in the z-direction for an acceleration of 16g. This displacement causes the movable electrode to move vertically between the fixed electrodes, which changes the overlap area of the capacitors. However, as mentioned above, this displacement causes the same change in the capacitance of Cup and Cdown, and no change is observed in the differential output of the sensor.

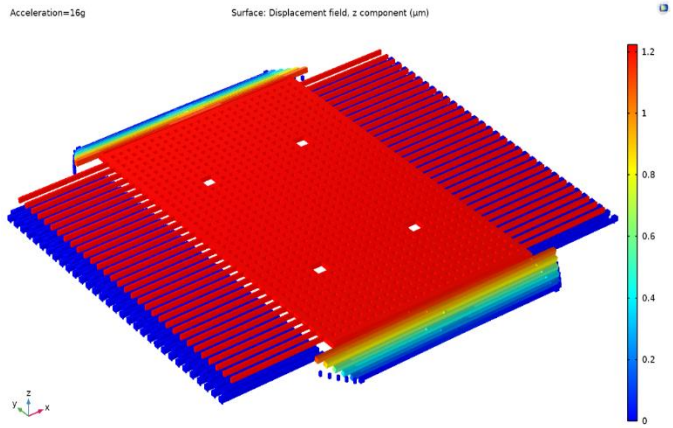


Figure 21. Displacement of moving mass per acceleration of 16g in z direction

**Minimum measurable acceleration**

One of the methods of determining the minimum measurable acceleration is using the thermal noise formula.

$$a_{min} = \sqrt{\frac{4k_bTC}{M_{eff}^2}} \qquad (9)$$


In this equation, $k_b$ is the Boltzmann constant, which is equal to $1.38064852 \times 10^{-23}\ \frac{m^2 kg}{s^2 {}^\circ K}$, and T is the temperature in Kelvin. The damping coefficient for squeeze film damping between two parallel plates is given by:

$$C = 7.2\mu_{eff} l \left(\frac{t}{d}\right)^3 \qquad (10)$$

In this equation, $l$ is the overlap length of the electrodes, $t$ is the overlap width of the electrodes, and $d$ is the gap between the electrodes. $\mu_{eff}$ is also known as the effective viscosity of air, and the value of this parameter for air at room temperature is $1.85 \times 10^{-5}\ kg/m.s$. According to the above equations, the accuracy of the accelerometer presented in this study is calculated to be $a_{min} = 3.8628\ \mu g/\sqrt{Hz}$.

**Bandwidth**

According to the lumped model, the dynamic equation of motion for the accelerometer can be expressed as:

$$M\frac{d^2y}{dt^2} + C\frac{dy}{dt} + Ky = F \qquad (11)$$

The force applied to the accelerometer at each stage is equal to one-sixth of the total acceleration $a_t = 16g$. Thus, the frequency response plotted using MATLAB software corresponds to the equivalent stiffness coefficients of the system at each stage. Figure (22) shows the frequency response of the proposed accelerometer.

$$F = ma = \frac{M_{eff} \times a_t}{6} \qquad (12)$$

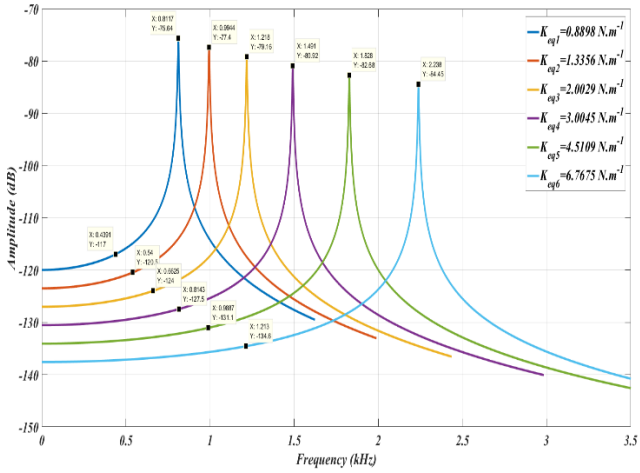


Figure 22. Frequency response

## Frequency Response:

For this purpose, Figure (22) is plotted in decibel scale. This figure shows the natural frequency of the accelerometer at each of the 6 stages. Also, considering the 3dB changes, the overall bandwidth of the system is more than 400 Hz at each of the 6 stages, and the system's performance in this region is completely uniform.

## Proposed Fabrication Process:

In this design, due to the use of surface micromachining technology, the type of wafer is not very important and only plays a supporting role. Therefore, we use a p-type silicon wafer with a thickness of 500 micrometers. Aluminum metal is usually used as a sacrificial layer for nickel, but for the movable mass, a sacrificial layer with a thickness of 5 micrometers is required, and creating this thickness using aluminum metal in a flat manner is not possible. PMMA photoresist can be used as a sacrificial layer.

1. Top and side views of the wafer

Figure 23. Silicon wafer

2. Thermal $SiO_2$ electric insulation layer with a thickness of less than $100nm$

Figure 24. Passivation layer

chrome sputtering as an interface layer with a thickness of $0.1\mu m$ and then nickel electroplating with a thickness of $0.9\mu m$ to create electrical connections

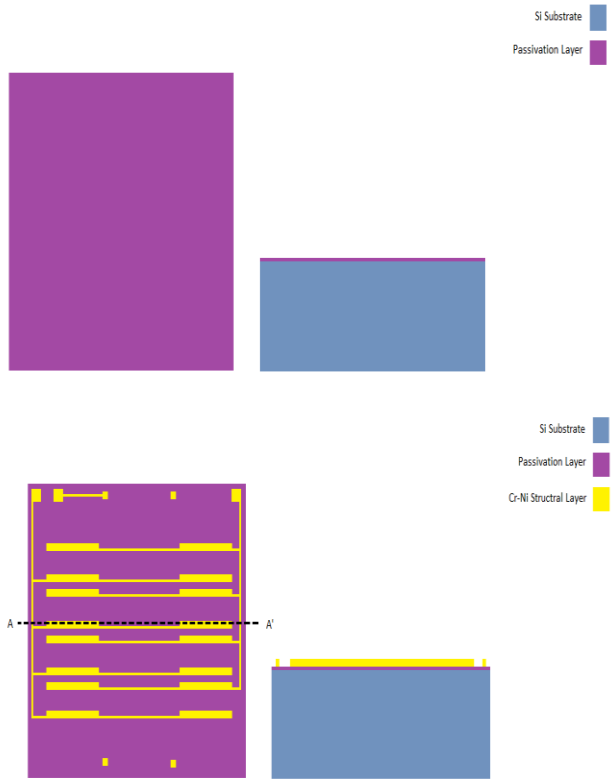


Figure 25. Electrical communication layer address

4. Second-stage electrical insulation layer to prevent short circuit between moving mass and electrical connections during operation

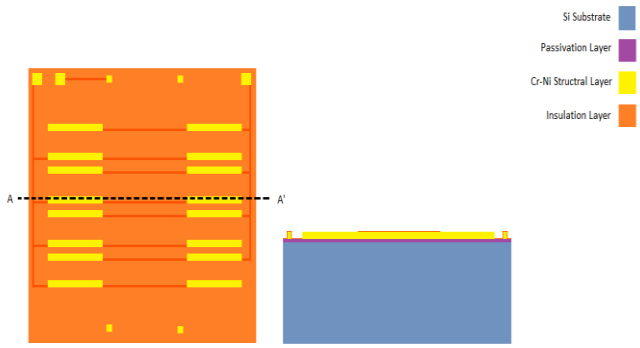


Figure 26. The insulation layer of the second stage

5. 5µm thick sacrificial layer address layer (PMMA) by spin on method and then a heating step for flattening


Figure 27. Sacrificial layer of the first stage

6- The second stage of masking in order to create an anchor pattern of springs and fixed electrodes

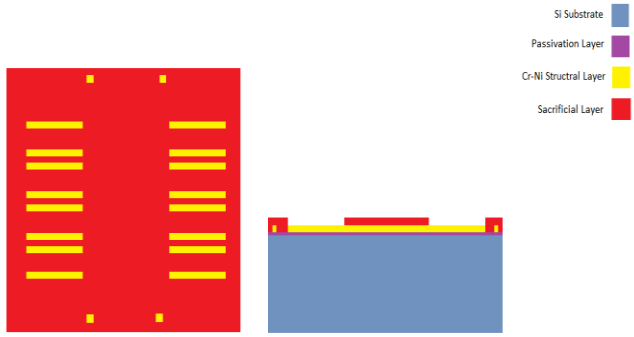


Figure 28. First stage masking

7. Nickel address layer by electroplating method in order to create fixed electrode anchors and springs and 5µm thick air gap.


Figure 29. Layer address of the structural layer of the first stage

8. 10μm thick sacrificial layer to create electrodes and moving mass


Figure 30. The sacrificial layer of the second stage

9- Masking to create moving electrodes along with other parts

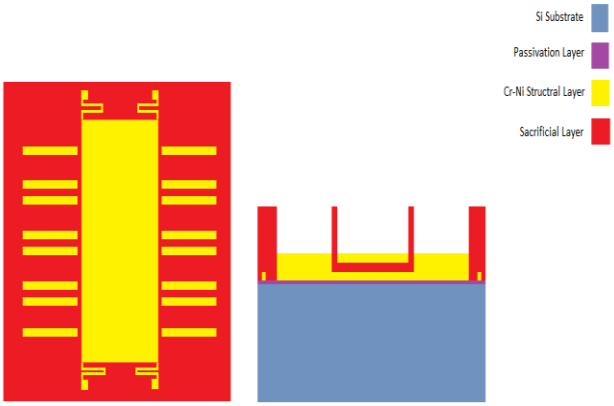


Figure 31. Creating a moving electrode pattern and other parts

10. Electroplating of 10μm thick nickel structural layer

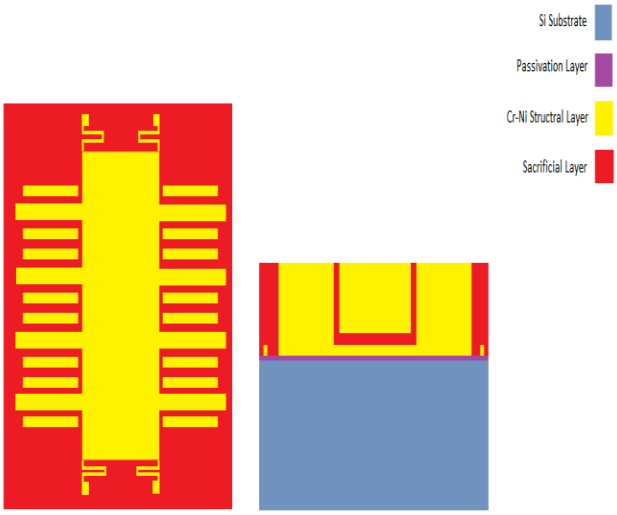


Shape. 32 second stage nickel address layer

11- Removing the sacrificial layer and releasing the structure using acetone solution

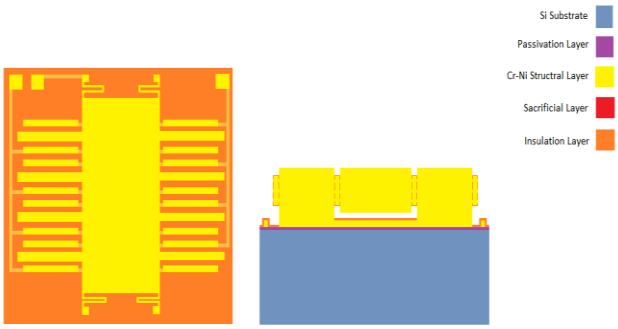


Figure 33. Removing the sacrificial layer and freeing the structure

## CONCLUSION:

The purpose of this research was to design an accelerometer using micromachining technology that would operate in a dynamic range of ±16 g. After careful consideration, a capacitive or electrostatic sensing mechanism was chosen for the implementation of the studied structure due to its numerous advantages over other conventional methods. The main focus of the researcher in this study was to present a method for optimizing and increasing sensitivity compared to previous studies. For this purpose, an intelligent and innovative method was employed in the design of the springs, which resulted in the achievement of the desired goal. The results of the simulations using both numerical and finite element methods confirm this. A summary of the activities carried out in the course of this study is presented below. It should be noted that the proposed method for designing the structure of the proposed accelerometer was considered with the minimum possible facilities in the micromachining process. In other words, by reducing the air gap between the electrodes to 3 micrometers during the micromachining process, it is possible to achieve a much higher capacitive sensitivity. This method is also applicable to the design of micromachined variable capacitor structures. To compare the performance of the proposed structure in this study with the research conducted by other researchers, Table (4) was prepared. This comparison attempts to highlight some of the research conducted in the field of capacitive accelerometers with capacitive mechanisms. Since research on accelerometers that are completely similar to the studied structure is not available in the existing literature, the comparison was made with structures with different dynamic ranges that have been published in recent years. However, from the comparison of the main performance parameters of the accelerometer in Table (4), it can be observed that the proposed structure in this study has a much better performance than other research.

Table 4. Comparison with other works

| Reference | Mechanism | Range | Resolution | Sensitivity | $C_0$ | Dimension | Tuning range |
|---|---|---|---|---|---|---|---|
| Khena | Diff- | ±2 | - | 800f | 10. | $1.32m$ | 30 |

| | | | | | | | |
|---|---|---|---|---|---|---|---|
| nisho et al. 2016 | capac itive | g | | F/g | 3pF | | % |
| Tahma sebipo ur et al. 2020 | Bulk-capac itive | ±1 00 g | $0.8\mu g/\sqrt{Hz}$ | 27.1 6fF/ g | 2.9 5pF | $16mm$ | - |
| Tez at al. 2015 | Bulk-capac itive | ±1 2g | $5.56\mu g/\sqrt{Hz}$ | - | 13. 2pF | $84mm$ | - |
| Mostaf azadeh et al. 2016 | Diff-capac itive | ±6 5g | $1.43\mu g/\sqrt{Hz}$ | 7fF/ g | - | $1.35m$ | 10 % |
| This work | Diff-capac itive | ±1 6g | $3.86\mu g/\sqrt{Hz}$ | 544f F/g | 1.8 36p F | $> 1mr$ | 90 % |

Accordingly, it is suggested to redesign using an air gap of less than 3 micrometers between the electrodes and check the dynamic behavior of the accelerometer in relation to the shock.

## REFERENCES:


1. Chen, H., et al. (2013). "Sliding mode control of a 2D torsional MEMS micromirror with sidewall electrodes." International Journal of Intelligent Mechatronics and Robotics (IJIMR) **3**(1): 16-26.
2. Fathalilou, M., et al. (2020). "Enhancement of the reliability of MEMS shock sensors by adopting a dual-mass model." Measurement **153**: 107428.
3. Ghasemi, S., et al. (2020). "On the mechanical behavior of a wide tunable capacitive MEMS resonator for low frequency energy harvesting applications." Microsystem Technologies: 1-10.
4. Goswami, Y., et al. (2021). "Performance Enhancement of a MEMS Capacitive Accelerometer Using Fuzzy Logic Controller." Journal of The Institution of Engineers (India): Series B **102**(2): 295-310.
5. Guo, Y., et al. (2020). "A stiffness-tunable MEMS accelerometer." Journal of Micromechanics and Microengineering **31**(2): 025005.
6. Khenanisho, A., et al. (2016). "Design and simulation of MEMS capacitive accelerometer in $\pm 2g$ range and resolution of mg." Thesis submitted to the University of Urmia for the degree of Master of Science.
7. Lu, M.-C .and G. K. Fedder (2004). "Position control of parallel-plate microactuators for probe-based data storage." Journal of microelectromechanical Systems **13**(5): 759-769.
8. Mobki, H., et al. (2020). "On the implementation of adaptive sliding mode robust controller in the stabilization of electrically actuated micro-tunable capacitor." Microsystem Technologies **26**: 3903-3916.
9. Mostafazadeh, A., et al., (2016) "Design and Simulation of MEMS Based Comb - Drive Accelerometer" Thesis submitted to the University of Urmia for the degree of Master of Science.
10. Nguyen, D., et al. (2010). "Fabrication and characterization of a wideband MEMS energy harvester utilizing nonlinear springs." Journal of Micromechanics and Microengineering **20**(12): 125009.
11. Qin ,Y., et al. (2017). Integral sliding mode based optimal composite nonlinear feedback control for capacitive micromachined ultrasonic transducers (CMUTs) system. 2017 36th Chinese Control Conference (CCC), IEEE.
12. Raman, J., et al. (2009). "A closed-loop digitally controlled MEMS gyroscope with unconstrained sigma-delta force-feedback." IEEE Sensors journal **9**(3): 297-305.
13. Sarraf, E. H., et al. (2012). "Novel band-pass sliding mode control for driving MEMS-based resonators." Sensors and Actuators A: Physical **186**: 154-162.
14. Sotoudeh, B. (2018). Design and Simulation of a wide range variable capacitor using electrostatic and piezoelectric actuations. Department of Electrical and Computer Engineering. Iran, URMIA UNIVERSITY. **Master of Science**.
15. Tahmasebipour, M., & Vafaie, A. (2020). "A novel single axis capacitive MEMS accelerometer with double-sided suspension beams fabricated using μWEDM." Sensors and Actuators A: Physical, 309, 112003.
16. Tez, S., Aykutlu, U., Torunbalci, M. M., & Akin, T. (2015). "A bulk-micromachined three-axis capacitive MEMS accelerometer on a single die." Journal of Microelectromechanical Systems, 24(5), 1264-1274.
17. Xin, M. and J. Fei (2015). "Adaptive vibration control for MEMS vibratory gyroscope using backstepping sliding mode control." Journal of Vibration and Control **21**(4): 808-817.
18. Zhu, G., et al. (2006). "Flatness-based control of electrostatically actuated MEMS with application to adaptive optics: A simulation study." Journal of microelectromechanical Systems **15**(5): 1165-1174.
19. Zwahlen, P., et al. (2010). Navigation grade MEMS accelerometer. 2010 IEEE 23rd international conference on micro electro mechanical systems (MEMS), IEEE.